

# Composition Directed Generation of Reactive Oxygen Species in Irradiated Mixed Metal Sulfides Correlated with Their Photocatalytic Activities

Weiwei He,\*†‡ Huimin Jia,† Dongfang Yang,† Pin Xiao,§ Xiaoli Fan,§ Zhi Zheng,\*† Hyun-Kyung Kim,|| Wayne G. Wamer,† and Jun-Jie Yin\*,†‡

†Key Laboratory of Micro–Nano Materials for Energy Storage and Conversion of Henan Province, Institute of Surface Micro and Nano Materials, Xuchang University, Xuchang, Henan 461000, P. R. China

‡Division of Bioanalytical Chemistry and Division of Analytical Chemistry, Office of Regulatory Science, Center for Food Safety and Applied Nutrition, U.S. Food and Drug Administration, College Park, Maryland 20740, United States

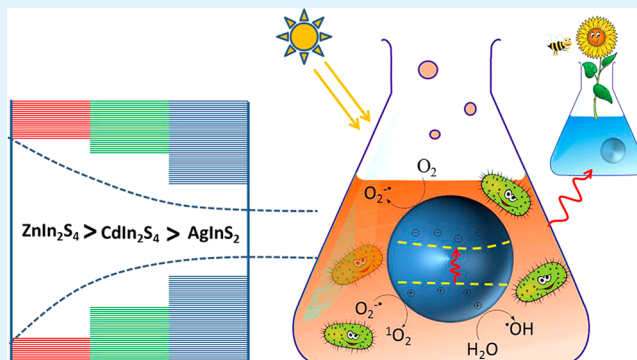
§School of Materials Science and Engineering, State Key Laboratory of Solidification Processing, Northwestern Polytechnical University, Xi'an, Shaanxi 710072, China

||Food Safety Bureau, Ministry of Food and Drug Safety, Osong Health Technology Administration Complex 363-700, Republic of Korea

## S Supporting Information

**ABSTRACT:** The ability of nanostructures to facilitate the generation of reactive oxygen species and charge carriers underlies many of their chemical and biological activities. Elucidating which factors are essential and how these influence the production of various active intermediates is fundamental to understanding potential applications of these nanostructures, as well as potential risks. Using electron spin resonance spectroscopy coupled with spin trapping and spin labeling techniques, we assessed 3 mixed metal sulfides of varying compositions for their abilities to generate reactive oxygen species, photogenerate electrons, and consume oxygen during photoirradiation. We found these irradiated mixed metal sulfides exhibited composition dependent generation of ROS:  $ZnIn_2S_4 > CdIn_2S_4 > AgInS_2$ .  $ZnIn_2S_4$  can generate  $\cdot OH$ ,  $O_2^-$  and  $^1O_2$ ;  $CdIn_2S_4$  can produce  $O_2^-$  and  $^1O_2$ , while  $AgInS_2$  only produces  $O_2^-$ . Our characterizations of the reactivity of the photogenerated electrons and consumption of dissolved oxygen, performed using spin labeling, showed the same trend in activity:  $ZnIn_2S_4 > CdIn_2S_4 > AgInS_2$ . These intrinsic abilities to generate ROS and the reactivity of charge carriers correlated closely with the photocatalytic degradation and photoassisted antibacterial activities of these nanomaterials.

**KEYWORDS:** reactive oxygen species, mixed metal sulfides, ESR, photocatalytic, antibacterial



## INTRODUCTION

As reactive oxygen species (ROS) play essential roles in environmental and biologic systems, the capabilities of micro and nano materials for mediating the generation of ROS have received significant interest.<sup>1,2</sup> These ROS typically include hydroxyl radicals ( $\cdot OH$ ), superoxide ( $O_2^-$ ), hydrogen peroxide ( $H_2O_2$ ), and singlet oxygen ( $^1O_2$ ). Although ROS are natural byproducts of the normal metabolism and function as important physiological regulators in cell signaling and homeostasis,<sup>3</sup> the overproduction of endogenous and exogenous ROS is known to cause significant damage to a variety of cellular structures,<sup>4</sup> resulting in aging and neurodegenerative diseases.<sup>5–7</sup> Nonetheless, ROS have been found to be therapeutically beneficial in killing pathogenic bacteria and cancer cells.<sup>8</sup> For example, when irradiated, Au nanoparticles

can generate singlet oxygen and therefore have been used as photothermal agents in treating cancerous tumors.<sup>9</sup>

The ability to trigger the production of ROS has been the dominant mechanism for understanding the various chemical and biological effects of nanomaterials. Notably, the formation of ROS during the incomplete reduction of oxygen or oxidation of  $H_2O$  is a crucial step in many photocatalytic and photoelectrochemical processes. This is clearly the case with  $ZnO$  nanostructures: the antibacterial and photocatalytic activities of  $ZnO$  nanocrystals have been attributed to their ability to produce ROS<sup>10,11</sup> and the deposition of metal

Received: April 26, 2015

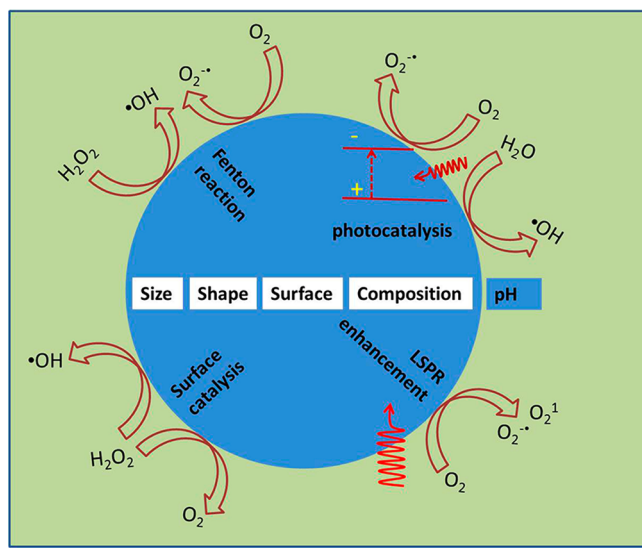
Accepted: July 9, 2015

Published: July 9, 2015

nanoclusters onto ZnO can greatly increase the amount of ROS generated, resulting in enhanced photocatalytic and photobiological activity.<sup>12,13</sup> Many micro and nano materials, including metal,<sup>14–16</sup> metal oxide and metal sulfide nanoparticles,<sup>10,11,17–19</sup> carbon nanomaterials,<sup>20</sup> and their hybrid counterparts,<sup>12,13,21</sup> are able to initiate the generation of ROS under varying experimental conditions. This suggests that the ability to promote ROS generation should be considered an intrinsic parameter of a given nanomaterial, similar to other physiochemical properties such as particle size, morphology, surface chemical state, and active surface area. In order to develop appropriate ROS-active nanomaterials for specific applications, we need a comprehensive understanding of how nanomaterials generate ROS.

Briefly, nanoparticles (NPs) generate ROS through 4 pathways (**Scheme 1**): (1) Fenton or Fenton-like reaction

**Scheme 1.** Mechanisms by Which NPs Can Generate ROS



between NPs and ROS ( $\text{H}_2\text{O}_2$  and superoxide),<sup>14,17</sup> (2) catalysis for generation and scavenging of ROS,<sup>14–16</sup> (3) surface plasmon resonance enhancement,<sup>9</sup> and (4) reaction with photogenerated charge carriers produced from photoexcitation of semiconductors.<sup>11–13,18,19</sup> In photocatalysis, it has been well established that semiconductor NPs absorb light resulting in the formation of an electron and hole pair, which in turn react with surrounding oxygen-containing substances leading to the generation of ROS. Any factor, such as particle size, composition, shape, chemical surface, and microenvironment, that influences the energy band structures, charge carrier separation efficiency, or other aspects of the pathway for ROS will affect the production of ROS. A few works have reported using the energy band gap to provide a possible explanation of how specific kinds of ROS can be generated from irradiated metal oxide and metal sulfide nanostructures, by analyzing the conduction/valence band energy positions with chemical redox potential of the corresponding ROS.<sup>22,23</sup> However, we still know very little about the relationships between the production of ROS and the physiochemical parameters of nanostructures (e.g., composition). This gap limits our understanding of potential ROS-related chemical and biological effects of nanomaterials. Our study specifically explores how the composition of nanomaterials affects ROS generation.

Detecting active intermediates such as ROS and photo-generated charge carriers is difficult, as these are very short-lived and extremely unstable entities, making it difficult to directly evaluate the abilities of nanomaterials to generate such active species. Often, analytic methods such as fluorescence or chemiluminescence are used for the determination of ROS. However, despite the simplicity and sensitivity of fluorescent and chemiluminescent probes for detecting ROS in vivo and in vitro, these methods have inherent disadvantages which can result in distracting artifacts,<sup>24,25</sup> making the precise identification of each type of ROS difficult. The most useful and powerful tool for determination of ROS formations in nanomaterials is Electron Spin Resonance (ESR),<sup>26</sup> because ESR can directly provide the specific spectrum associated with the paramagnetic characteristic for each ROS spin adduct and spin label. We have demonstrated the usefulness of spin trapping and spin labeling techniques in ESR in our previous studies on (1) the interaction between nanomaterials and ROS in biologically relevant systems,<sup>14,15</sup> (2) the events involving ROS generation and scavenge triggered by nanomaterials with/without assistance of light,<sup>11–21</sup> and (3) electron transfer behaviors and reactivity.<sup>18–20</sup> This method provides us with many conveniences for identifying active intermediates induced by nanostructures and accessing their activity.

We studied NPs of three indium-based mixed metal sulfides (MMS):  $\text{ZnIn}_2\text{S}_4$  (ZIS),  $\text{CdIn}_2\text{S}_4$  (DIS), and  $\text{AgInS}_2$  (AIS), which exhibit varied compositions, distinct energy band structures, and good visible light responses for photocatalysis. Using these MMS as models, we examined the relationships among chemical compositions, energy band positions, photo-generated electron/hole pairs, and ROS generation, and also looked for correlations between the photocatalytic and photoinduced antibacterial activities of these metal sulfides irradiated with visible light. Using ESR techniques coupled with spin trapping and spin labeling, we identified not only what kind and how many ROS were produced by these MMS, but also quantitatively analyzed the dissolved oxygen consumption and reactivity of the photogenerated electrons during the photocatalytic process.

## EXPERIMENTAL SECTION

**Chemical and Materials.** Analytically pure cadmium chloride, indium(III) chloride, zinc nitrate, bismuth chloride, sulfur, and absolute ethanol were purchased from Shanghai Chemical Reagent Co. Ltd. (Shanghai, China). The spin-trap *S*-*tert*-butoxycarbonyl-*S*-methyl-1-pyrroline-*N*-oxide (BMPO) was purchased from Applied Bioanalytical Laboratories (Sarasota, FL). 3-Carbamoyl-2,2,5,5-tetramethyl-3-pyrroline-1-yloxy (CTPO) and 2,2,6,6-tetramethylpiperidine-1-oxyl (TEMPO) were purchased from Alexis, Enzo Life Sciences, Inc. (NY, U.S.). 4-Oxo-2,2,6,6-tetramethylpiperidine (4-Oxo-TEMP), Rhodamine B, salicylic acid (SA),  $\text{NaN}_3$ , DMSO, superoxide dismutase (SOD), diethylenetriaminepentaacetic acid (DTPA), xanthine, xanthine oxidase, and standard buffer solutions were all purchased from Sigma-Aldrich (St. Louis, MO). Milli-Q water (18  $\text{M}\Omega \text{ cm}$ ) was used for preparation of all solutions.

**Synthesis of  $\text{ZnIn}_2\text{S}_4$ ,  $\text{CdIn}_2\text{S}_4$ , and  $\text{AgInS}_2$  MMS.** In a typical synthesis, metal ions (0.25 mmol  $\text{CdCl}_2$ , or 0.25 mmol  $\text{Zn}(\text{NO}_3)_2$ , or 0.5 mmol  $\text{Ag}_2\text{S}$ ), 0.5 mmol  $\text{InCl}_3$  and 2 mmol thioacetamide were mixed with 21 mL  $\text{H}_2\text{O}$  (or 21 mL DMF for  $\text{AgInS}_2$ ) under vigorous stirring. The resulting mixture was transferred into a 28 mL Teflon-lined stainless steel autoclave. This autoclave was sealed, heated at 160 °C for 16 h, and then air-cooled to room temperature. Finally, the precipitate was collected by centrifugation, washed 2 times with water and 1 time with ethanol, and then dried under vacuum at 50 °C.

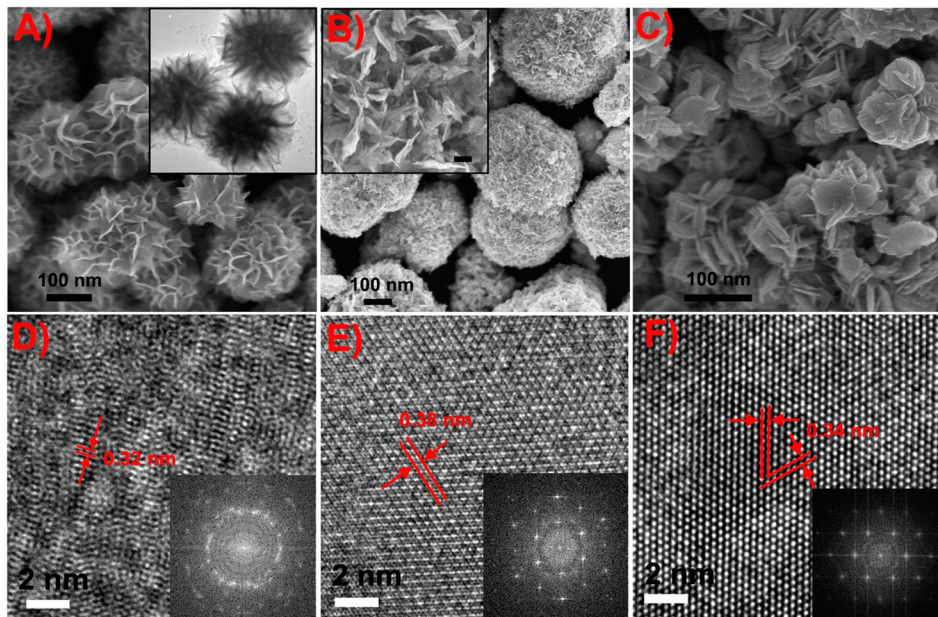


**Figure 1.** SEM images of ZIS (A), DIS (B), and AIS (C); HRTEM images of ZIS (D), DIS (E), and AIS (F). The inset in A is the TEM image of ZIS; the inset in B shows the higher magnification SEM image. The insets in D, E, and F show the corresponding FFT images.

**Characterization.** Transmission electron microscopy (TEM) and high resolution TEM (HRTEM) images were captured on a JEM 2100 FEG (JEOL) transmission electron microscope (accelerating voltage of 200 kV) located at the NanoCenter (University of Maryland, College Park, MD). The crystal structure of synthesized mixed-metal sulfides was characterized by X-ray diffraction (XRD, Bruker D8 Advance diffractometer) with monochromatized Cu K $\alpha$  radiation ( $\lambda = 1.5418 \text{ \AA}$ ). A Varian Cary 5000 spectrophotometer was used to perform UV-vis diffuse reflection spectroscopy. The BET surface area of each MMS was determined by the nitrogen adsorption method, using a Gemini 2380 specific area analyzer (Micromeritics, Norcross, GA). All X-ray photoelectron spectroscopy (XPS) experiments were performed using the synchrotron radiation XPS at the Photoelectron Station (Beijing Synchrotron Radiation Facility, Beijing, China). Measurements were carried out in an ultrahigh vacuum chamber with background pressures of  $1 \times 10^{-9}$  Torr. C 1s at 285.5 eV to calibrate the charge effect of the samples.

The photocatalytic activities of our  $\text{ZnIn}_2\text{S}_4$ ,  $\text{CdIn}_2\text{S}_4$  and  $\text{AgInS}_2$  MMS were assessed by measuring their effects on the degradation of Rhodamine B (RhB) and salicylic acid (SA) under visible light. 0.1 mg/mL of each potential MMS was dispersed in a 20 mL aqueous solution containing 0.1 mg/L RhB or 0.5 mM SA. Each sample mixture was magnetically stirred for 30 min to establish an adsorption-desorption equilibrium between the photocatalyst and substrates prior to exposure to light. After that, a 300 W xenon lamp, filtered to deliver light above 400 nm, was used to irradiate the sample solution. The solution was stirred during irradiation to maintain a suspension. At selected time intervals (15 min), 3 mL aliquots of suspension were removed and centrifuged. The residual concentration of the RhB or SA in the supernatant was monitored using a Varian Cary 5000 spectrophotometer.

**Growth of Bacteria and Evaluation of Antibacterial Activity of  $\text{ZnIn}_2\text{S}_4$ ,  $\text{CdIn}_2\text{S}_4$ , and  $\text{AgInS}_2$ .** Pure bacterial cultures of *Staphylococcus aureus* subsp. *aureus* (ATCC 29213) were chosen as model organisms for antibacterial activity experiments. These bacteria were grown overnight on Brain Heart Infusion Agar (BHIA, BD-Difco) plates in an incubator at 37 °C. Bacterial growth was harvested using a sterilized swab, then resuspended in the 0.01 × PBS buffer to achieve a viable cell concentration of about  $1.5 \text{ to } 2.0 \times 10^9 \text{ cells/mL}$ . This suspension of bacteria was used as a stock suspension for our antibacterial activity tests.

The antibacterial activities of MMS NPs were tested in 96-well plates. 180  $\mu\text{L}$  of the bacterial stock suspension was transferred into each well, then 20  $\mu\text{L}$  of 0.5 mg/mL  $\text{ZnIn}_2\text{S}_4$ ,  $\text{CdIn}_2\text{S}_4$ , or  $\text{AgInS}_2$  was added to each well. The 96-well plates containing bacteria and nanomaterials were irradiated under a solar simulator (Model 91190–1000, Oriel, Stratford, CT) for 10 min and then incubated at 37 °C for 1 h. The bacteria and nanomaterial mixture in each well was serially diluted, and then 10  $\mu\text{L}$  from each dilution was spread onto BHIA agar plates. These plates were incubated at 37 °C overnight, and the resulting bacterial growth was enumerated in colony forming units (CFU). The bacteria survival rate was calculated as follows:

$$\text{survival rate}(\%) = 100 \times \text{CFU}(\text{cell + nano + rad}) / \text{CFU}_0(\text{cell})$$

where CFU (cell + nano + rad) is the number of colony-forming units measured after plating cells irradiated in the presence of nanomaterials, and CFU<sub>0</sub> (cell) is the number of colony-forming units measured after plating cells that were not exposed to either nanomaterials or to simulated sunlight. All tests were conducted in triplicate and repeated at least twice to confirm reproducibility.

**Electron Spin Resonance Spectroscopy.** A Bruker EMX ESR spectrometer (Billerica, MA) was used at room temperature for all the ESR measurements, and 450 W xenon lamp filtered to generate visible light (above 400 nm) was used as the irradiation source. 50  $\mu\text{L}$  aliquots of control or sample solutions were put into quartz capillary tubes with internal diameters of 0.9 mm and sealed. The capillary tubes were inserted into the ESR cavity, and sample spectra were recorded at selected times during the radiation period. To detect the different ROS and electrons generated during the irradiation of the MMS solutions, 25 mM BMPO was used as a spin trap to verify the formation of superoxide ( $\cdot\text{OOH}$ ), hydroxyl radicals ( $\cdot\text{OH}$ ), 10 mM 4-oxo-TEMP was selected to demonstrate the production of singlet oxygen, and 0.1 mM TEMPO was used as a spin label for studying electrons. In these experiments, the intensity of the ESR signal was measured as the peak-to-peak height of the second line of ESR spectrum. The spectra of control samples that either did not contain any metal-sulfide photocatalyst or had not been exposed to irradiation were also recorded.

We used ESR spin label oximetry with the water-soluble spin label CTPO to assess oxygen consumption during irradiation of  $\text{ZnIn}_2\text{S}_4$ ,  $\text{CdIn}_2\text{S}_4$ , and  $\text{AgInS}_2$ , since the superhyperfine structural change in the ESR spectrum of CTPO is also a sensitive measure of changes in  $\text{O}_2$  concentration. Therefore, the ESR spectrum of CTPO was used to

calculate O<sub>2</sub> concentrations. Other settings for ESR measurements were as follows: 1 G field modulation, 100 G scan range, 20 mW microwave power for detection of spin adducts using spin traps, 0.04 G field modulation, 5 G scan range, and 1 mW microwave power for ESR oximetry using the spin label CTPO.

## RESULTS AND DISCUSSION

### Formation of ZnIn<sub>2</sub>S<sub>4</sub>, CdIn<sub>2</sub>S<sub>4</sub>, and AgInS<sub>2</sub> MMS.

Controlling the composition of alloyed semiconductors appears to be an effective way to tune their band gap energy, photocatalytic properties,<sup>27</sup> and probably, their ability to generate ROS. Three MMS were synthesized via a simple and effective hydrothermal method. Figure 1 displays the typical SEM images of prepared ZIS, DIS, and AIS. Although these 3 metal sulfides show different morphologies, their general dimensions are on the submicro scale and are built up from hierarchical nanoscale structures. For example, the flower-like ZIS particles have an average diameter of approximately 200 nm, consisting of “petals” with thickness of ~5 nm. In contrast, the DIS spheres and AIS structures are composed of plate-like components with thickness of approximately 10 nm. We verified the elemental composition of these structures (Zn/In/S in ZIS, Cd/In/S in DIS, and Ag/In/S in AIS) using EDX (data not shown). High resolution TEM images show details of each crystal structure (ZIS, DIS, and AIS). Figure 1D shows the HRTEM image of ZIS, showing that the lattice fringes were well-resolved, with planar spacing of 0.32 nm, which corresponds the distance between (102) facets of ZnIn<sub>2</sub>S<sub>4</sub>. The corresponding Faster Fourier Transform (FFT) image (inset in Figure 1D) shows the rings that consist of diffraction spots, indicating a polycrystalline structure of the ZIS “nanopetal”. Results from HRTEM confirm that each nanopetal is composed of small nanocrystals with preferential but different orientations. Both the HRTEM images and FFT images of DIS and AIS showed well-resolved lattice fringes with good arrangement, confirming the crystalline structures of DIS and AIS. The lattice spacing of 0.38 nm in Figure 1E and 0.34 nm in Figure 1F corresponds the distance between (220) planes of DIS and (002) planes of AIS, respectively. Figure 2 summarizes the X-ray powder diffraction (XRD) results. The XRD pattern from DIS shows that all the diffraction peaks can be indexed to cubic cadmium indium sulfide (JCPDS no. 27–60). The XRD patterns for ZIS and AIS samples matched quite well with hexagonal zinc indium sulfide (JCPDS no. 72–773) and

orthorhombic silver indium sulfide (JCPDS no. 25–1328), respectively. No other peaks characteristic of impurities were detected, indicating the excellent crystallinity of these mixed metal sulfide nanostructures.

The XPS spectra of ZIS, CIS, and AIS nanostructures are provided in Supporting Information (SI) Figure S1. The XPS spectra indicate that all three metal sulfides show the signals from C 1s, S 2p, In 3d, and O 1s. The C 1s at 285.5 eV and O 1s at 532 eV comes primarily from the molecules (e.g., TAA) used to prepare the metal sulfide structures or from the oxygen and oxygen containing species chemisorbed to the surface of samples. The binding energy of S 2p (161.8 eV) and In 3d (In 3d5/2 at 445.0 and In 3d3/2 at 452.5 eV) indicate the coexistence of S and In in the chemical states of S<sup>2-</sup> and In<sup>3+</sup>. Also, each MMS exhibits clear signals from Ag 3d for AIS, Zn 2p for ZIS, and Cd 3d for DIS, confirming the presence of Ag, Zn and Cd in the corresponding MMS. In addition, the high resolution XPS spectra (SI Figure S2) indicate the binding energy of Ag 3d5/2 (367.8 eV), Ag 3d3/2 (373.8 eV), Cd 3d5/2 (405 eV), Cd 3d 3/2 (411.7 eV), Zn 2p3/2 (1022.8 eV), and Zn 2p1/2 (1045.7 eV), and the orbital separations are calculated as 6.0, 6.7, and 22.9 eV for Ag 3d, Cd 3d and Zn 2p, respectively. These results indicate that the chemical states of Ag, Cd and Zn are in the form of Ag<sup>+</sup>, Cd<sup>2+</sup> and Zn<sup>2+</sup>.<sup>28,29</sup>

The UV-vis-NIR diffuse reflectance spectra of our ZIS, DIS and AIS MMS (SI Figure S3), all show adsorption cutoffs longer than 400 nm and extend longer than 800 nm, suggesting these materials are responsive to visible light or near-infrared light. These spectra also clearly indicate that the chemical compositions of each MMS had a large effect on absorption properties. Taking the properties of In<sub>2</sub>S<sub>3</sub> as a baseline, the absorption edges for ZIS shifted from 580 nm to about 450 nm and for DIS, the edge shifted to about 550 nm; AIS made the absorption edge shift longer, to about 750 nm. The energy band gaps ( $E_g$ ) were estimated from the absorption plots by using the formula,  $a\text{hv} = A (\text{hv} - E_g)^{1/2}$ , where  $\alpha$  is the absorption coefficient and  $\text{hv}$  is the photon energy. The optical band gaps for ZIS, DIS, and AIS were determined to be 2.5, 2.1, and 1.5 eV, respectively. Using different metallic elements to create sulfide NPs will result in materials with considerably different energy band structures, which may, in turn, greatly influence the amount of photoactivity these materials will exhibit.

**Distinct Ability of ZIS, DIS, and AIS to Generate Reactive Oxygen Species during Irradiation.** A spin trap, BMPO, was used to verify the generation of superoxide or hydroxyl radicals produced from MMS. The spin adduct BMPO/<sup>•</sup>OOH formed between BMPO and superoxide, and the adduct BMPO/<sup>•</sup>OH formed between BMPO and hydroxyl radicals, displayed distinctive ESR spectra which could be identified easily by analyzing their ESR spectra. Figure 3 shows the ESR spectra obtained for samples containing BMPO and each of our MMS before and during irradiation. Samples that contained only irradiated BMPO, and the control samples which contained BMPO and MMS in the absence of irradiation, showed no detectable ESR spectra. However, samples containing mixtures of BMPO and nanostructures that were irradiated with visible light for 3 min, did show ESR spectra characteristic for the superoxide spin adduct, displaying a four-line ESR spectrum with relative intensities of 1:1:1:1 and hyperfine splitting parameters of  $a_N = 13.4$ ,  $a_H^{\beta} = 12.1$  G, (Figure 3). These results indicate that these three mixed metal sulfides could generate superoxide after excitation with visible light. The

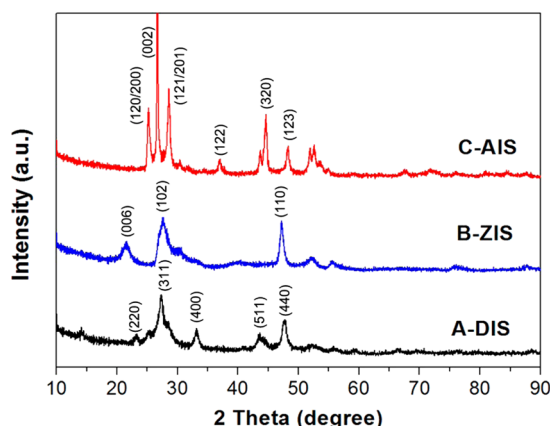
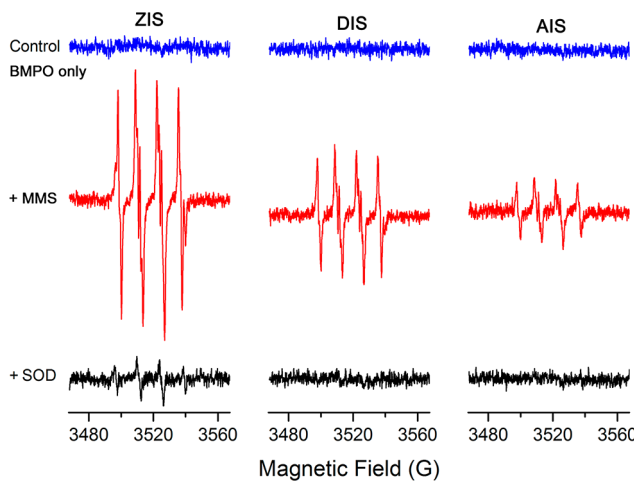


Figure 2. XRD patterns for prepared CdIn<sub>2</sub>S<sub>4</sub>, ZnIn<sub>2</sub>S<sub>4</sub>, and AgInS<sub>2</sub> nanostructures.



**Figure 3.** Production of superoxide and/or hydroxyl radicals from  $\text{ZnIn}_2\text{S}_4$ ,  $\text{CdIn}_2\text{S}_4$ , and  $\text{AgInS}_2$  nanostructures irradiated with visible light. These ESR spectra were obtained from samples containing 25 mM BMPO only, and mixed with 0.1 mg/mL metal sulfides nanostructures in the absence and presence of 2 U/mL SOD. All the spectra were recorded during irradiation for 3 min with visible light.

ESR signal intensity suggested their activity in producing superoxide followed the order:  $\text{ZnIn}_2\text{S}_4 > \text{CdIn}_2\text{S}_4 > \text{AgInS}_2$ .

Superoxide dismutase (SOD) can efficiently scavenge superoxide, which has often been used to indirectly demonstrate the formation of superoxide.<sup>15,16</sup> In this experiment, once 2 U/mL SOD was added to irradiated samples containing ZIS nanostructures, the ESR signal from BMPO/ $\cdot\text{OOH}$  was significantly reduced; when SOD was added to the irradiated samples containing DIS or AIS, ESR signals were totally quenched. These results further demonstrate the generation of superoxide from the irradiated ZIS, DIS, and AIS nanostructures. It was noteworthy that in the case of ZIS after addition of SOD, the weak ESR signal remained and possessed a four-line ESR spectrum with relative intensities of 1:2:2:1 and hyperfine splitting parameters of  $a_N = a_H = 14.9$  G, which was characteristic for the spin adduct of BMPO/ $\cdot\text{OH}$ .<sup>30</sup> The ESR spectra of BMPO/ $\cdot\text{OOH}$  and BMPO/ $\cdot\text{OH}$  overlap, thus the ESR signal from weak hydroxyl radical cannot be identified before addition of SOD. By using BMPO as spin trap and SOD as scavenger, we confirmed that superoxide and hydroxyl radicals were generated from  $\text{ZnIn}_2\text{S}_4$ , and only superoxide from  $\text{CdIn}_2\text{S}_4$  and  $\text{AgInS}_2$  nanostructures under visible light.

Singlet oxygen formed in the presence of photoexcited metal sulfide was detected by using 4-oxo-TEMP, a spin trap which reacts with singlet oxygen to produce 4-oxo-2,2,6,6-tetramethylpiperidine-N-oxyl (TEMPONE), a nitroxide radical having a distinctive ESR response. This signal can be used to demonstrate whether the mixed metal sulfides photocatalyze the formation of singlet oxygen. Figure 4 displays the ESR spectra from samples containing 4-oxo-TEMP and MMS with and without irradiation. No ESR signal was observed for samples containing only the 4-oxo-TEMP or unirradiated metal sulfides. In contrast, a three line spectrum with relative intensity ratio of 1:1:1 and calculated hyperfine splitting 15.85 G characteristic for the nitroxide radical, TEMPONE, was observed for irradiated samples containing ZIS or DIS. No ESR signal was evident in the presence of AIS. To confirm the ESR signal attributed to singlet oxygen, we further investigated

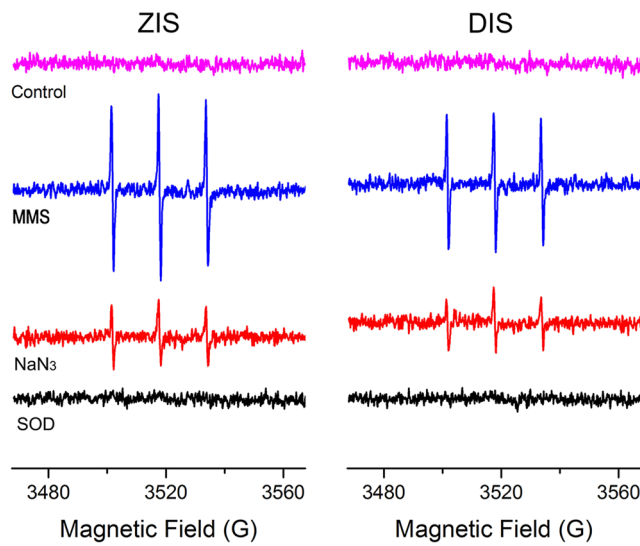


**Figure 4.** Singlet oxygen formed during visible light irradiation of ZIS and DIS. ESR spectra were obtained at room temperature from samples containing 10 mM 4-oxo-TEMP only with irradiation (control), and mixed with 0.1 mg/mL ZIS or DIS under irradiation in the absence and presence of 10 mM  $\text{NaN}_3$  or 2 U/ml SOD. All the spectra were recorded during irradiation for 5 min with visible light.

the effect of  $\text{NaN}_3$ , a specific singlet oxygen quencher, on the TEMPONE ESR signal. We observed that addition of 10 mM  $\text{NaN}_3$  resulted in the significant reduction of the TEMPONE ESR signal during photoexcitation of DIS or ZIS (Figure 4). These results demonstrate that DIS and ZIS photocatalyze the formation of singlet oxygen. In our previous works, we have demonstrated that the singlet oxygen from photoirradiated  $\text{ZnS}$  or  $\text{ZnO}$  nanoparticles resulted from the reaction between superoxide and holes.<sup>16,19</sup> Does the singlet oxygen from these MMS go through the similar mechanism? To answer this question, we tested the effect of SOD on the TEMPONE signal from ZIS and DIS. The addition of 2 U/ml SOD resulted in the complete inhibition of the ESR signal of 4-oxo-TEMP generated from irradiated ZIS and DIS (Figure 4). Because SOD does not react with singlet oxygen and has no effect on the signal of TEMPONE, these results confirm the formation of singlet oxygen through a reaction involving superoxide.

As discussed above, use of the ESR spin trap technique combined with the scavenging method enables easy detection of each separate ROS produced dynamically from photoexcited ZIS, DIS, and AIS, which had previously been considered a great challenge, since ROS are a diverse set of short-lived and chemically distinct entities. In addition, we have used spin labels, which can interact with free electrons or paramagnetic molecules (dioxygen) resulting in corresponding changes of their ESR spectra, to predict the photogenerated electrons from photoexcited semiconductors and oxygen consumption.

**Photogenerated Electrons and Oxygen Consumption during Photocatalytic Reaction Measured by ESR-Spin Labeling.** ESR-spin labeling, a classic technique used in study of biological dynamics, is an effective tool for probing the electrons generated by irradiated metal oxide or metal sulfide semiconductors.<sup>11,18</sup> The spin label, TEMPO, was employed in spin labeling because of several advantages: (1) good solubility in aqueous environment, (2) stability against light irradiation, and (3) having no interaction with all kinds of oxidants formed in photocatalysis, such as hydroxyl radical, superoxide, singlet

oxygen, and holes. In our system, the change of the inherent ESR signal of TEMPO is an obligatory indicator for the electron transfer between TEMPO and photoexcited semiconductors. The reduction of TEMPO by electrons produces an ESR silent molecule, TEMPOH, and leads to the reduction of intensity and flattening of the ESR signal. This is the basis for characterizing the photoinduced electrons from semiconductors using ESR-spin labeling. Figure 5 shows the changes of

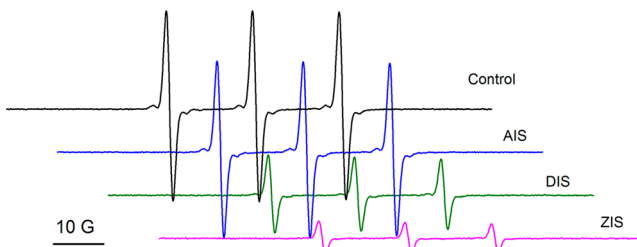


**Figure 5.** Photogenerated electrons from different MMS during irradiation with visible light. ESR spectra were obtained from samples containing 0.02 mM TEMPO only with exposure to visible light (control), TEMPO mixed with MMS during irradiation in the presence of 0.1 mg/mL AIS, DIS, and ZIS. All the spectra were recorded after 5 min irradiation with light above 400 nm.

TEMPO signal in the interaction with different photoexcited MMS. The ESR signal of TEMPO kept nearly unchanged when exposed to light only or mixed with ZIS, DIS, or AIS in the dark. Under visible light for 3 min, ZIS or DIS caused an evident reduction, 82.5% for ZIS and 58.8% for DIS, of the ESR signal intensity while AIS only reduced slightly the intensity of TEMPO signal. Extension of irradiation for MMS results in the continuous reduction of TEMPO signal until the TEMPO molecules were totally consumed (data not shown). Since the consumption of TEMPO can be correlated closely with the photogenerated electrons on the surface of MMS, thus the level of electrons produced from irradiated of ZIS, DIS, and AIS and their reducing ability order can be estimated as follows:  $ZnIn_2S_4 > CdIn_2S_4 > AgInS_2$ .

Subtle changes in dissolved oxygen will have a profound effect on the generation of some ROS (e.g., superoxide and singlet oxygen) and oxidative reactions. To monitor the oxygen consumption during the photocatalysis assisted by metal sulfides, ESR oximetry in conjunction with the spin label CTPO, a sensitive method to detect dissolved oxygen, was employed here. ESR oximetry is based on the bimolecular collision between spin label and dioxygen ( $O_2$ ). Because  $O_2$  is paramagnetic, this physical collision between  $O_2$  and spin label molecules produces spin exchange, leading to a shorter relaxation time for the spin label and in turn resulting in ESR signal with broader line width and lower intensity. Therefore, it is feasible to determine in real-time the change of  $O_2$  by ESR. CTPO was chosen as spin label because its superhyperfine structure of ESR signal is quite sensitive to oxygen variation at a low concentration. Increasing the concentration of oxygen will result in less evident superhyperfine structure (inset in Figure 6B). The ESR spectra of CTPO have three lines because of the hyperfine interaction of unpaired electrons with the nitrogen nucleus. In this work, the first line of hyperfine structure of CTPO at 3500 G was recorded for calculating changes in oxygen concentrations. Figure 6A shows, for example, the evolution of the ESR spectra of CTPO versus the visible light irradiation time in the presence of  $CdIn_2S_4$ . The CTPO ESR

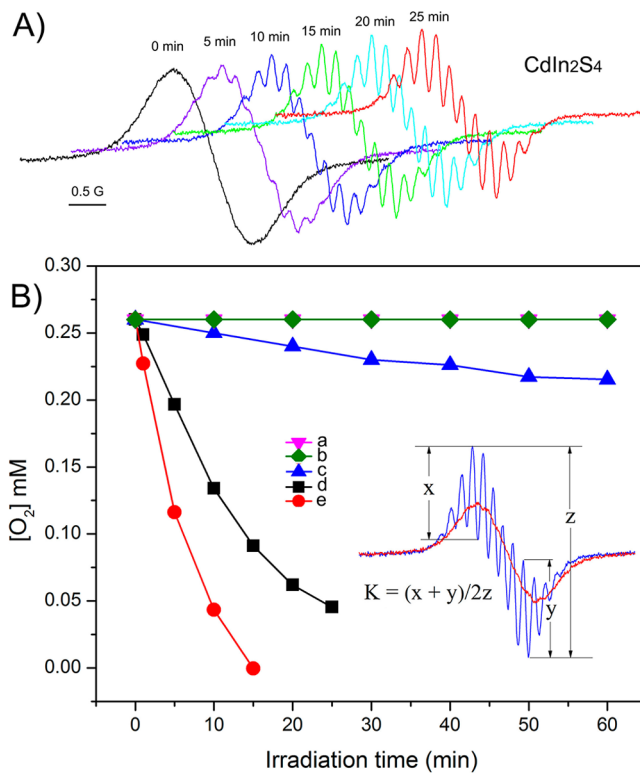


**Figure 6.** Oxygen consumption during the photoirradiation of metal sulfides. (A) Evolution of ESR spectrum of 0.1 mM CTPO during irradiation with visible light in the presence of 0.1 mg/mL  $CdIn_2S_4$ ; (B) The dissolved oxygen consumption during irradiation in the absence (a) and presence of 0.1 mg/mL  $AgInS_2$  (c),  $CdIn_2S_4$  (d), and  $ZnIn_2S_4$  (e), b represents the control containing photocatalysts but without light. Inset in (B) illustrates the method for calculation of the  $K$  value from ESR spectrum which was used to calculate the concentration of oxygen remained in solution.

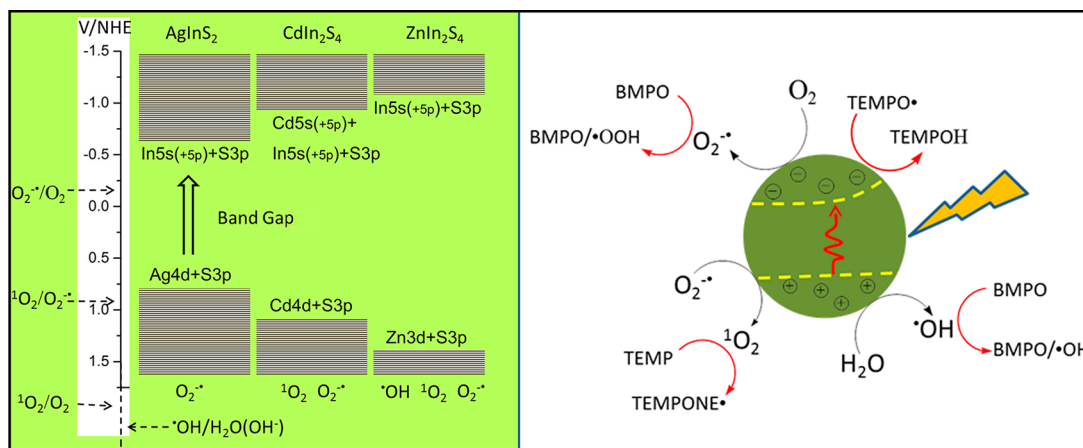
signal exhibits a smooth line without super hyperfine structures before irradiation because the sample is saturated with oxygen. The super hyperfine characteristic of CTPO spectra clearly appeared after 5 min irradiation of DIS, and the spectra become sharper and the super hyperfine structure split clearer at longer irradiation times, indicating that less oxygen remained to interact with CTPO molecules. The  $K$  parameter is calculated from the super hyperfine structures by the equation  $K = (x + y)/2z$  (inset in Figure 6B) and is used to determine oxygen concentration by following equation:<sup>31</sup>

$$[O_2](mM) = 0.23 - 0.746K$$

Figure 6B shows the comparison of changes in oxygen during photoexcitation of different metal sulfides with the control. No changes in oxygen concentrations were observed in the control experiments (without catalysts) for both the irradiated and nonirradiated samples. This indicates that oxygen consumption was associated closely with the photoexcited MMS, as the production of superoxide and singlet oxygen required the molecular oxygen. Using same amount of catalyst, the MMS exhibiting the strongest ability to react with oxygen during irradiation was ZIS, which used up the available oxygen in 15 min. The trend for oxygen consumption followed the same pattern as for the photoexcitation of electrons and generating superoxide or singlet oxygen: ZIS > DIS > AIS.

**Composition Directed the Generation of ROS from Photoexcited MMS.** ESR spin trapping and spin labeling

**Scheme 2.** Energy Band Distribution of ZIS, DIS, and AIS Compared with Chemical Redox Potentials of ROS; Right Cartoon Shows the Formation and Detection of ROS Produced from Irradiated Semiconductors



techniques allow access to direct and specific information about ROS, photogenerated electrons, and molecular oxygen. The three MMS exhibit distinct abilities in ROS production and reducing power: ZIS can generate superoxide, hydroxyl radicals, and singlet oxygen, DIS produces superoxide, and singlet oxygen, while AIS only generates superoxide. This suggests that an effective means of tailoring the reducing activity and generation of ROS would be to change the metallic composition of nanoparticles meant to serve in semiconductors.

Changing the composition of semiconductor nanostructures would also change the band gaps, crystal structures, and electronic structures exhibited by these materials, in turn changing their optical and catalytic properties.<sup>32,33</sup> The reactivity of charge carriers and ROS produced by photoexcited semiconductors are mostly determined by the band gap and the energy band positions of the valence band and conduction band. The electrochemical driving force for triggering generation of ROS is from the redox potential difference between energy band positions (valence band or conduction band) and standard redox potential of ROS. In aqueous media, the reduction potential for dissolved oxygen/superoxide couple ( $O_2(aq)/O_2^{-\bullet}$ ) is  $-0.16$  eV,<sup>34</sup> singlet oxygen/dioxygen ( $O_2^1/O_2$ ) is  $1.88$  eV,<sup>22</sup> singlet oxygen/superoxide ( $O_2^1/O_2^{-\bullet}$ ) is  $0.97$  eV and for the  $H_2O/\cdot OH$  couple is  $2.2$  eV.<sup>22,35</sup> Therefore, in order for an irradiated semiconducting nanostructure to form superoxide and hydroxyl radical, it must have a conduction band edge position more negative than  $-0.16$  eV and have a valence band edge position more positive than  $2.2$  eV. We have measured the energy band gaps for ZIS, DIS, and AIS. The conduction band edge and valence band edge of mixed metal sulfides were calculated using the following equations:<sup>36</sup>

$$E_v = X_{MIS} + 0.5E_g + 0.059(pH_{ZPC} - pH) + E_0$$

$$\begin{aligned} E_c &= E_v - E_g \\ &= X_{MIS} - 0.5E_g + 0.059(pH_{ZPC} - pH) + E_0 \end{aligned}$$

where  $E_v$  refers to valence band edge energy at pH 6.0, the pH photocatalytic reactions occurred;  $X_{MIS}$  is the absolute electronegativity for each mixed sulfide,  $X_{MIS}$  ( $M_xIn_yS_z$ ) =  $(X_M^x X_I^y X_S^z)^{1/(x+y+z)}$ , where  $X_M$ ,  $X_I$ ,  $X_S$  are the absolute electronegativity of the atoms M, In, and S;<sup>37</sup>  $pH_{ZPC}$  is the point of zero zeta-potential for each mixed sulfide, which is available in the literature;  $E_0$  is scale factor to the absolute

vacuum scale ( $E_0 = -0.45$  eV for normal hydrogen electrode). The band edge positions of conduction band and valence band of 3 mixed metal sulfides are illustrated in Scheme 2. The  $E_c$  energy of ZIS, DIS, and AIS ( $-1.1$ ,  $-0.95$ , and  $-0.69$  V with respect to NHE) is more negative than redox potential of  $O_2(aq)/O_2^{-\bullet}$ , therefore each of these 3 mixed sulfides favor the generation of superoxide. The  $E_v$  energy of ZIS, DIS, and AIS are calculated to be  $1.4$ ,  $1.15$ , and  $0.81$  eV, respectively. Compared with reduction potentials of  $0.95$  eV ( $^1O_2/O_2^{-\bullet}$ ), ZIS and DIS possess more positive valence band edge than  $^1O_2/O_2^{-\bullet}$ , thus electron transfer between holes and superoxide to form singlet oxygen is favorable for both photoexcited ZIS and DIS. AIS cannot generate singlet oxygen, as the holes in its valence band ( $E_v = 0.81$  eV) are insufficiently oxidative to form singlet oxygen. A comparison of  $E_v$  with either  $H_2O/\cdot OH$  (+2.2 eV) or  $HO^-/\cdot OH$  (+1.9 eV), shows that the  $E_v$  for all 3 mixed sulfides are less than  $1.9$  eV, indicating that they are not likely to form hydroxyl radicals. Nonetheless, we detected the generation of hydroxyl radicals from irradiated ZIS by using BMPO as spin trap. This finding may indicate that additional factors influence whether ROS can be generated. It has been suggested that the hydroxyl radicals can be formed via a one electron reduction of  $H_2O_2$ , which could be produced by trapping an electron of superoxide in  $ZnIn_2S_4$  photocatalytic systems.<sup>38</sup> If this mechanism is active, then hydroxyl radicals should also be generated by photoexcited DIS and AIS since both of them can produce superoxide; however, we did not detect any such hydroxyl radicals during our investigations of DIS or AIS.

We have also examined the abilities of binary metal sulfide nanostructures ( $ZnS$ ,  $CdS$ ,  $In_2S_3$ , and  $Ag_2S$ ) for generating ROS when irradiated:  $ZnS$  could generate hydroxyl radicals, superoxide, and singlet oxygen,  $CdS$  can generate singlet oxygen and superoxide but not hydroxyl radicals,  $In_2S$  and  $Ag_2S$  only produce superoxide.<sup>14</sup> These results confirm that the amount of ROS generated by irradiated semiconductors is determined by their chemical compositions and band structures. On the basis of these findings, it is reasonable to propose a hypothesis that if the MMS exhibit similar electronic structure to binary metal sulfides they may behave similarly in producing ROS. We further calculated the contribution of each element to the energy band distributions of MMS by adopting hybrid density functional theory (SI Figure S4). The density contour maps of ZIS, DIS, and AIS indicated that the top of

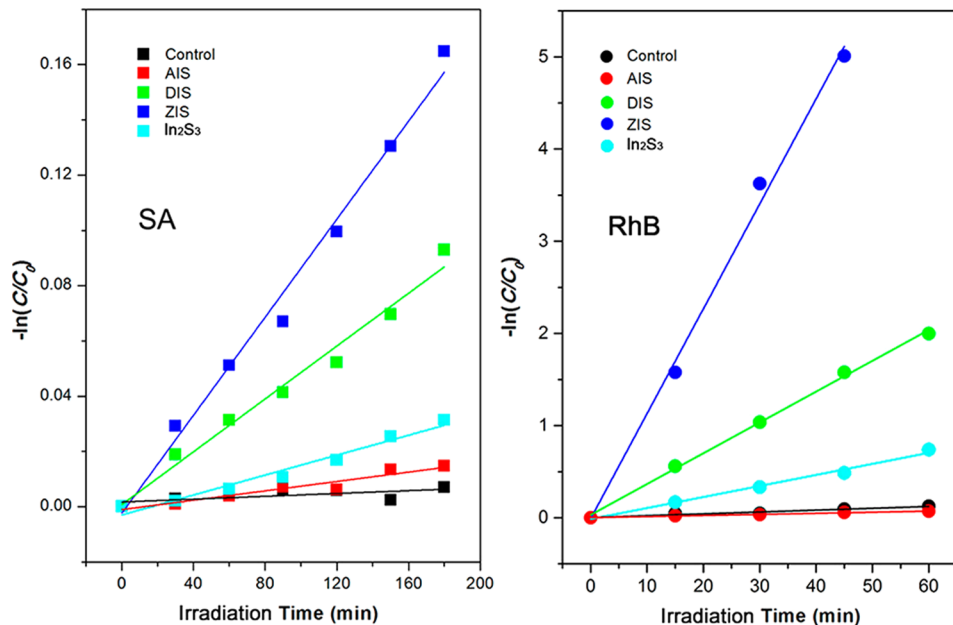


**Figure 7.** Photocatalytic activity of ZIS, DIS, AIS, and  $\text{In}_2\text{S}_3$  for degrading RhB and SA under visible light. The concentration of catalysts is fixed at 0.1 mg/mL.

valence band were composed of predominantly Zn 3d and S 3p, Cd 4d and S 3p, and Ag 4d and S 3p, respectively. The conduction band was dominated by In 5s, In 5p, and S 3p. Particles of ZIS possess the valence band structure adapting to ZnS, thus may exhibit similar ability to ZnS in generating hydroxyl radicals; DIS possesses the valence band structure adapting to CdS thus exhibits similar abilities to produce singlet oxygen. We have observed that ZIS, DIS, and AIS have differing capacities for producing electrons and exhibiting photo-reduction ability; we believe these results from their conduction band edge position, which determines the fate of photo-generated electrons.

**Photocatalytic and Antibacterial Activities.** The distinctive abilities of our MMS for generating active intermediates may make them useful for both environmental remediation and antibacterial purposes. Therefore, we further tested and compared the how well ZIS, DIS, and AIS were able to photocatalyze the degradation of pollutants and kill pathogenic bacteria. Two representative pollutants, the organic dye rhodamine B (RhB) and the colorless molecule salicylic acid (SA), were selected as degradation targets to evaluate the photocatalytic activities of ZIS, DIS, and AIS under visible light (Figure 7 and SI Figure S5). For comparison,  $\text{In}_2\text{S}_3$  was also examined. Figure 7 shows  $-\ln(C/C_0)$  as a function of irradiation time during the degradation in the absence and presence of  $\text{In}_2\text{S}_3$ , ZIS, DIS, and AIS, which indicates the pseudo-first order kinetic process of the photocatalytic degradation of both SA and RhB. The control experiments without any photocatalysts show that SA and RhB are resistant to degradation by visible light. In contrast, adding any of the four metal sulfides shows considerable ability to degrade SA and RhB in the presence of visible light. For example, the SA degradation rate constants for ZIS, DIS,  $\text{In}_2\text{S}_3$ , and AIS were determined to be 8.87, 4.78, 1.8, and  $0.8(\times 10^{-4}) \text{ min}^{-1}$ , respectively. The RhB degradation rate constants for ZIS, DIS, and  $\text{In}_2\text{S}_3$  were determined to be 0.11, 0.03, and  $0.01 \text{ min}^{-1}$ , respectively; AIS showed very weak photocatalytic activity, which was comparable to the control condition. These results

indicate that (1) the four metal sulfides share the same trend in decreasing photocatalytic activity for degrading SA and RhB: ZIS > DIS > IS > AIS, and (2) these metal sulfides exhibited higher photocatalytic activity for RhB than SA. These results match well with the ESR results for the production of ROS.

To compare the antibacterial activity of photoexcited ZIS, DIS, and AIS, the Gram-positive *Staphylococcus aureus* (*S. aureus*) was selected as a representative bacterium (Figure 8). In the absence of mixed metal sulfides, *S. aureus* grew well either in the dark or under light irradiation conditions (Control 1). Exposure to ZIS, DIS, and AIS nanostructures without irradiation resulted in a slight decrease in bacterial survival; this may have been due to general toxic effects caused by physical

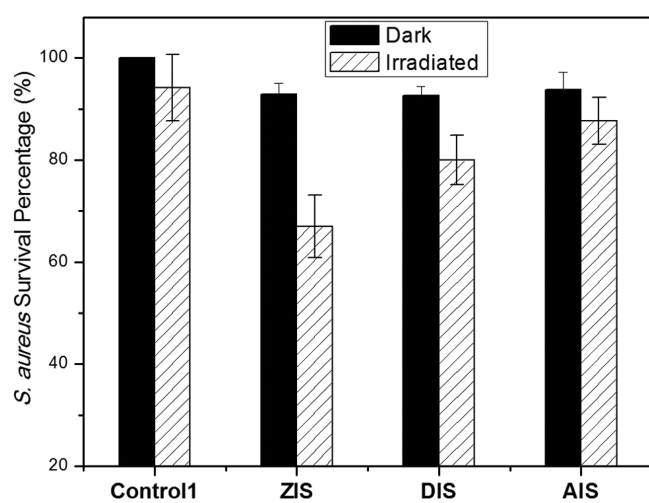


**Figure 8.** Ability of ZIS, DIS, and AIS to kill *S. aureus* after irradiation for 10 min. Control represents bacteria that were not exposed to any nanostructures under either dark or light conditions. Within the column for each nanostructure type, we provide results for those bacteria exposed to 0.05 mg/mL nanostructures alone (“Dark”) or exposed to 10 min of light (“Irradiated”).

interactions between cellular structures and the NPs. After exposure to both MMS and irradiation with visible light for 10 min, *S. aureus* survival decreased considerably (Figure 8). This indicates that light exposure is the more significant source for the antibacterial activities of these metal sulfide nanostructures. We found that extending the irradiation time resulted in further decreases in the survival of *S. aureus* (data not shown). We observed that the activity of 3 MMS in killing *S. aureus* followed the order: ZIS > DIS > AIS; this is in agreement with the results of ESR experiments and photocatalytic trend.

As discussed above, photoexcited ZIS was most effective in producing all the active intermediates, including the kinds and amounts of ROS, photogenerated electrons, and consumption of dissolved oxygen; DIS and AIS were consistently ranked second and third in our tests. While we cannot detail the contribution of individual ROS and holes/electrons to the whole photocatalytic reaction and antibacterial effect, the results from both ESR and photocatalytic experiments demonstrate that these photocatalytic and antibacterial activities are correlated closely with the generation of ROS (category and amount) and reactivity of photogenerated charge carriers from photoexcited metal sulfides. Since the molecular compositions and energy band structures influence the generation of ROS and charge carriers of semiconductors, our results also imply an effective way to predict the photocatalytic and photoinducible antibacterial activity of nanostructures.

## CONCLUSIONS

We explored the photocatalytic and antimicrobial activities of three MMS,  $ZnIn_2S_4$ ,  $CdIn_2S_4$ , and  $AgInS_2$  and investigated the effects of chemical composition on the generation of reactive oxygen species and electrons. When irradiated,  $ZnIn_2S_4$  can generate hydroxyl radicals, superoxide, and singlet oxygen,  $CdIn_2S_4$  can produce both superoxide and singlet oxygen; however,  $AgInS_2$  only produces superoxide. Intriguingly, the same activity trend is shown in the interactions between these mixed-metal sulfides and photoexcited electrons and reduction of dissolved oxygen:  $ZnIn_2S_4 > CdIn_2S_4 > AgInS_2$ . These specific ESR results on active intermediates from photoexcited mixed metal sulfides were found to correlate closely with the photocatalytic activities such as degrading organic pollutants and killing bacteria. Since the ROS, oxygen and electron transfer have critical roles in photocatalysis, biological chemistry, and photocurrent conversion, our results will be valuable in the design and testing of nanomaterials for applications in photocatalysis and biomedicine.

## ASSOCIATED CONTENT

### Supporting Information

(Figure S1) XPS spectra of  $AgInS_2$ ,  $ZnIn_2S_4$ , and  $CdIn_2S_4$ ; (Figure S2) high resolution XPS spectra of AIS (a), DIS (b), and ZIS (c) in the range of  $Ag_3d$ ,  $Cd_3d$ , and  $Zn_2p$ , respectively; (Figure S3) (a) UV-vis-NIR diffuse reflectance spectra of as-prepared ternary ZIS, DIS, and AIS; (Figure S4) density contour maps for the LUMO and HOMO of  $ZnIn_2S_4$ ,  $CdIn_2S_4$ , and  $AgInS_2$ ; (Figure S5) photocatalytic activity of  $In_2S_3$ ,  $ZnIn_2S_4$ ,  $CdIn_2S_4$ , and  $AgInS_2$  toward degradation of rhodamine B (a) and salicylic acid (b) under visible light irradiation; and method detail for calculation. The Supporting Information is available free of charge on the ACS Publications website at DOI: 10.1021/acsami.5b03626.

## AUTHOR INFORMATION

### Corresponding Authors

\*E-mail: heweiweixu@gmail.com (W.H.).  
\*E-mail: zhengzhi99999@gmail.com (Z.Z.).  
\*E-mail: junjie.yin@fda.hhs.gov (J.-J.Y.).

### Notes

The authors declare no competing financial interest.

## ACKNOWLEDGMENTS

This work was supported by National Natural Science Foundation of China (Grant No. 21303153 and 61204009), Program for Science & Technology Innovation Talents in Universities of Henan Province (14HASTIT008), Innovation Scientists and Technicians Troop Construction Projects of Henan Province (Grant No. 144200510014), and a regulatory science grant under the FDA Nanotechnology CORES Program and by the Office of Cosmetics and Colors, CFSAN/FDA. The authors thank Dr. Lili Fox Vélez for editorial and scientific writing support.

## REFERENCES

- (1) Lee, S. H.; Gupta, M. K.; Bang, J. B.; Bae, H.; Sung, H. J. Current Progress in Reactive Oxygen Species (ROS)-Responsive Materials for Biomedical Applications. *Adv. Healthcare Mater.* **2013**, *2*, 908–915.
- (2) Yan, L.; Gu, Z.; Zhao, Y. Chemical Mechanisms of the Toxicological Properties of Nanomaterials: Generation of Intracellular Reactive Oxygen Species. *Chem. - Asian J.* **2013**, *8*, 2342–2353.
- (3) Ray, P. D.; Huang, B. W.; Tsuji, Y. Reactive Oxygen Species (ROS) Homeostasis and Redox Regulation in Cellular Signaling. *Cell. Signalling* **2012**, *24*, 981–990.
- (4) Stadtman, E. R.; Berlett, B. S. Reactive Oxygen-mediated Protein Oxidation in Aging and Disease. *Drug Metab. Rev.* **1998**, *30*, 225–243.
- (5) Sohal, R. S.; Mockett, R. J.; Orr, W. C. Mechanisms of Aging: An Appraisal of the Oxidative Stress Hypothesis. *Free Radical Biol. Med.* **2002**, *33*, 575–586.
- (6) Butterfield, D. A. Alzheimer's A-amyloid Peptide and Free Radical Oxidative Stress. In *Reactive Oxygen Species in Biological Systems: An Interdisciplinary Approach*, 1<sup>st</sup> ed.; Colton, C., Gilbert, D., Eds.; Kluwer Academic Publishers: New York, 1999; pp 609–638.
- (7) Cohen, G. Oxidative Stress and Parkinson's Disease. In *Reactive Oxygen Species in Biological Systems: An Interdisciplinary Approach*, 1<sup>st</sup> ed.; Gilbert, D. L., Colton, C. A., Eds.; Kluwer Academic Publishers: New York, 1999; pp 593–608.
- (8) Zhou, D.; Shao, L.; Spitz, D. R. Chapter One – Reactive Oxygen Species in Normal and Tumor Stem Cells. *Adv. Cancer Res.* **2014**, *122*, 1–67.
- (9) Vankayala, R.; Kuo, C. L.; Sagadevan, A.; Chen, P. H.; Chiang, C. S.; Hwang, K. C. Morphology Dependent Photosensitization and Formation of Singlet Oxygen ( $^1\Delta_g$ ) by Gold and Silver Nanoparticles and Its Application in Cancer Treatment. *J. Mater. Chem. B* **2013**, *1*, 4379–4387.
- (10) Applerot, G.; Lipovsky, A.; Dror, R.; Perkas, N.; Nitzan, Y.; Lubart, R.; Gedanken, A. Enhanced Antibacterial Activity of Nanocrystalline ZnO Due to Increased ROS-Mediated Cell Injury. *Adv. Funct. Mater.* **2009**, *19*, 842–852.
- (11) He, W.; Zhao, H.; Jia, H.; Yin, J.-J.; Zheng, Z. Determination of Reactive Oxygen Species from ZnO Micro-nano Structures with Shape-dependent Photocatalytic Activity. *Mater. Res. Bull.* **2014**, *53*, 246–250.
- (12) He, W. W.; Kim, H.-K.; Wamer, W. G.; Melka, D.; Callahan, J. H.; Yin, J.-J. Photogenerated Charge Carriers and Reactive Oxygen Species in ZnO/Au Hybrid Nanostructures with Enhanced Photocatalytic and Antibacterial Activity. *J. Am. Chem. Soc.* **2014**, *136*, 750–757.
- (13) He, W. W.; Wu, H.; Wamer, W. G.; Kim, H.-K.; Zheng, J.; Jia, H.; Zheng, Z.; Yin, J.-J. Unraveling the Enhanced Photocatalytic

- Activity and Phototoxicity of ZnO/Metal Hybrid Nanostructures from Generation of Reactive Oxygen Species and Charge Carriers. *ACS Appl. Mater. Interfaces* **2014**, *6*, 15527–15535.
- (14) He, W. W.; Zhou, Y. T.; Wamer, W. G.; Boudreau, M. D.; Yin, J. J. Mechanisms of the pH Dependent Generation of Hydroxyl Radicals and Oxygen Induced by Ag Nanoparticles. *Biomaterials* **2012**, *33*, 7547–7555.
- (15) He, W. W.; Zhou, Y. T.; Wamer, W. G.; Hu, X.; Wu, X.; Zheng, Z.; Boudreau, M. D.; Yin, J. J. Intrinsic Catalytic Activity of Au Nanoparticles with Respect to Hydrogen Peroxide Decomposition and Superoxide Scavenging. *Biomaterials* **2013**, *34*, 765–773.
- (16) Liu, Y.; Wu, H.; Li, M.; Yin, J.-J.; Nie, Z. H. pH dependent Catalytic Activities of Platinum Nanoparticles with Respect to the Decomposition of Hydrogen Peroxide and Scavenging of Superoxide and Singlet oxygen. *Nanoscale* **2014**, *6*, 11904–11910.
- (17) Dong, J.; Song, L.; Yin, J.-J.; He, W.; Wu, Y.; Gu, N.; Zhang, Y. Co<sub>3</sub>O<sub>4</sub> Nanoparticles with Multi-Enzyme Activities and Their Application in Immunohistochemical Assay. *ACS Appl. Mater. Interfaces* **2014**, *6*, 1959–1970.
- (18) He, W. W.; Jia, H.; Wamer, W. G.; Zheng, Z.; Li, P.; Callahan, J. H.; Yin, J.-J. Predicting and Identifying Reactive Oxygen Species and Electrons for Photocatalytic Metal Sulfide Micro–nano Structures. *J. Catal.* **2014**, *320*, 97–105.
- (19) Jia, H.; He, W.; Wamer, W. G.; Han, X.; Zhang, B.; Zhang, S.; Zheng, Z.; Xiang, Y.; Yin, J.-J. Generation of Reactive Oxygen Species, Electrons/Holes, and Photocatalytic Degradation of Rhodamine B by Photoexcited CdS and Ag<sub>2</sub>S Micro-Nano Structures. *J. Phys. Chem. C* **2014**, *118*, 21447–21456.
- (20) Zhang, W.; Wang, C.; Lu, Z.; Yin, J.-J.; Zhou, Y.-T.; Gao, X.; Fang, Y.; Nie, G.; Zhao, Y. Unraveling Stress-induced Toxicity Properties of Graphene Oxide and the Underlying Mechanism. *Adv. Mater.* **2012**, *24*, 5391–5397.
- (21) Li, M.; He, W.; Liu, Y.; Wu, H.; Wamer, W. G.; Lo, Y. M.; Yin, J.-J. FD&C Yellow No. 5 (Tartrazine) Degradation via Reactive Oxygen Species Triggered by TiO<sub>2</sub> and Au/TiO<sub>2</sub> Nanoparticles Exposed to Simulated Sunlight. *J. Agric. Food Chem.* **2014**, *62*, 12052–12060.
- (22) Li, Y.; Zhang, W.; Niu, J.; Chen, Y. Mechanism of Photogenerated Reactive Oxygen Species and Correlation with the Antibacterial Properties of Engineered Metal-Oxide Nanoparticles. *ACS Nano* **2012**, *6*, 5164–5173.
- (23) Zhang, H.; Ji, Z.; Xia, T.; Meng, H.; Low-Kam, C.; Liu, R.; Pokhrel, S.; Lin, S.; Wang, X.; Liao, Y.; Wang, M.; Li, L.; Rallo, R.; Damoiseaux, R.; Telesca, D.; Mädler, L.; Cohen, Y.; Zink, J.; Nel, A. Use of Metal Oxide Nanoparticle Band Gap To Develop a Predictive Paradigm for Oxidative Stress and Acute Pulmonary Inflammation. *ACS Nano* **2012**, *6*, 4349–4368.
- (24) Kalyanaraman, B.; Darley-Usmar, V.; Davies, K. J. A.; P. Dennery, A.; Forman, H. J.; Grisham, M. B.; Mann, G. E.; Moore, K.; Roberts, L. J., II; Ischiropoulos, H. Measuring Reactive Oxygen and Nitrogen Species with Fluorescent Probes: Challenges and Limitations. *Free Radical Biol. Med.* **2012**, *52*, 1–6.
- (25) Kobayashi, H.; Gil-Guzman, E.; Mahran, A. M.; Sharma, R. K.; Nelson, D. R.; Thomas, A. J., Jr; Agarwal, A. Quality Control of Reactive Oxygen Species Measurement by Luminol-Dependent Chemiluminescence Assay. *J. Androl.* **2001**, *22*, 568–574.
- (26) He, W. W.; Liu, Y. T.; Wamer, W. G.; Yin, J. J. Electron Spin Resonance Spectroscopy for the Study of Nanomaterial-mediated Generation of Reactive Oxygen Species. *J. Food Drug Anal.* **2014**, *22*, 49–63.
- (27) Regulacio, M. D.; Han, M.-Y. Composition-Tunable Alloyed Semiconductor Nanocrystals. *Acc. Chem. Res.* **2010**, *43*, 621–630.
- (28) Chen, Z. X.; Ren, Z. Y.; Xu, J.-J.; Xiao, G. C.; He, Y.-H. Hydrothermal Synthesis of CdIn<sub>2</sub>S<sub>4</sub> and Photocatalytic Degradation of Methyl Orange under Visible-light Irradiation. *Chin. J. Struct. Chem.* **2012**, *31*, 1815–1822.
- (29) Peng, S.; Li, L.; Wu, Y.; Jia, L.; Tian, L.; Srinivasan, M.; Ramakrishna, S.; Yan, Q.; Mhaisalkar, S. G. Size- and Shape-controlled Synthesis of ZnIn<sub>2</sub>S<sub>4</sub> Nanocrystals with High Photocatalytic Performance. *CrystEngComm* **2013**, *15*, 1922.
- (30) Zhao, H. T.; Joseph, J.; Zhang, H.; Karoui, H.; Kalyanaraman, B. Synthesis and Biochemical Applications of A Solid Cyclic Nitronate Spin Trap: A Relatively Superior Trap for Detecting Superoxide Anions and Glutathiol Radicals. *Free Radical Biol. Med.* **2001**, *31*, 599–606.
- (31) Zhou, Y. T.; Yin, J. J.; Lo, Y. M. Application of ESR Spin Label Oximetry in Food Science. *Magn. Reson. Chem.* **2011**, *49*, S10Se12.
- (32) Zhuang, X.; Ning, C. Z.; Pan, A. Composition and Bandgap-Graded Semiconductor Alloy Nanowires. *Adv. Mater.* **2012**, *24*, 13–33.
- (33) Zhao, Z.-Y.; Dai, W.-W. Structural, Electronic, and Optical Properties of Eu-Doped BiOX (X = F, Cl, Br, I): A DFT+U Study. *Inorg. Chem.* **2014**, *53*, 13001–13011.
- (34) Wood, P. M. The Potential Diagram for Oxygen at pH 7. *Biochem. J.* **1988**, *253*, 287–289.
- (35) Mayeda, E. A.; Bard, A. J. Production of Singlet Oxygen in Electrogenerated Radical Ion Electron Transfer Reactions. *J. Am. Chem. Soc.* **1973**, *95*, 6223.
- (36) Xu, Y.; Schoonen, M. A. A. The Absolute Energy Positions of Conduction and Valence Bands of Selected Semiconducting Minerals. *Am. Mineral.* **2000**, *85*, 543–556.
- (37) Pearson, R. G. Absolute Electronegativity and Hardness: Application to Inorganic Chemistry. *Inorg. Chem.* **1988**, *27*, 734–740.
- (38) Chen, Z.; Li, D.; Zhang, W.; Shao, Y.; Chen, T.; Sun, M.; Fu, X. Photocatalytic Degradation of Dyes by ZnIn<sub>2</sub>S<sub>4</sub> Microspheres under Visible Light Irradiation. *J. Phys. Chem. C* **2009**, *113*, 4433–4440.